Geochemical Perspectives Letters

Temperature dependence of magmatic iron-redox speciation to 2100 °C

S.P. Aithala, C.A. Macris, M.M. Hirschmann

Supplementary Information

The Supplementary Information includes:

- 1. Methods
- 2. Results
- 3. Recalculating experiments to common oxygen fugacity and melt composition
- 4. Applying temperature Equations 7–9 to model silicate liquids of differing compositions and f_{O2}s
- Tables S-1 to S-5
- Figures S-1 to S-3
- Supplementary Information References

1. Methods

Experimental Methods

We synthesised an FeO*-rich basaltic starting composition with ~15.2 wt. % FeO* (with 10 % of FeO* added as $^{57}Fe_2O_3$ to aid Mössbauer analyses) modified from the parental magma composition of Gusev Crater basalt, "Humphrey" (McSween *et al*., 2006). Details regarding synthesis of Humphrey are in Aithala *et al*. (2026).

As previously reported in Aithala *et al*. (2026), we conducted 6 experiments on the Humphrey in a Deltech VT-28 HN-C gas-mixing furnace at the University of Minnesota – Twin Cities in air ($\log f_{O2} \equiv -0.68$) at 1250, 1300, 1365, 1400, 1450, and 1500 °C at 72, 24, 6, 6, 2, and 1 h, respectively, to ensure sufficient time for chemical equilibration at low temperatures, and to mitigate volatile loss at high temperatures (Table S-1). Details regarding the calibration of Type S and Type B thermocouples, and the SIRO2 C700+ Solid Zirconia Electrolyte oxygen sensor can be found in Aithala *et al*. (2026). Experimental charges consisted of ~30–35 mg of Humphrey powder bonded to Pt wire using hydrated polyvinyl alcohol (PVA). As these experiments were conducted at oxidizing conditions, Fe loss from the silicate to the Pt was minimal. The experiments were terminated rapidly by quenching in deionised water. The experimental assemblages were then sectioned by tungsten wire saw to produce multiple chips for analysis.

Higher temperature experiments were conducted with an Aerodynamic Laser Levitation Furnace (ALLF) at Indiana University Indianapolis, equipped with a conical gas nozzle and a 400-watt CO_2-laser (Ni *et al*. 2021). First, ~10–15 mg of Humphrey was packed in 1 mm diameter hemisphere wells in a copper hearth plate and fused to spheroids by heating to superliquidus temperatures by laser for two 8–15 s laser pulses at 8–12 %. Previous studies have shown that this brief fusion step does not measurably alter sample composition, even for moderately volatile elements, and is thus suitable for spheroid preparation prior to levitation (Ni *et al*., 2021; Young *et al*., 2022). These spheroids were then levitated in ultra-high purity (UHP) O_2 gas (Airgas UHP300; 99.994 % purity, with total impurities <10 ppm) flowing at 300–340 cc/min and laser-heated to fully melt the sample and to equilibrate with the levitating gas atmosphere under fixed f_{O2}.

Experimental temperatures ranging from 1800–2100 °C (Table S-1) were achieved at 100 °C/s by automated ramping of laser power. Sample temperatures were measured using a Chino IR-CAS single-wavelength pyrometer operating at 0.9 µm and configured with an emissivity setting of 0.92. This value is supported by multiple high-temperature measurements of basaltic melts and rocks, which consistently report near-infrared emissivities of ~0.90–0.95. Spectral emissivity measurements at 0.85–1.2 µm on natural and synthetic basalts at elevated temperatures (~470 °C) confirm $\varepsilon \approx 0.95$ (Helbert *et al*., 2017; Dyar *et al*., 2017, 2019a,b). These results are consistent with higher-temperature studies on fully molten basaltic compositions, which report stable emissivities of 0.92–0.95 across the 0.9–2.5 µm range (Treiman *et al*., 2019; Lombardo *et al*., 2020; Biren *et al*., 2022). Taken together, these data support the use of $\varepsilon = 0.92$ as a representative value for basaltic melts under oxidizing conditions in aerodynamic levitation experiments. The pyrometer readings were used to dynamically control the laser power and maintain target temperatures during levitation.
The experimental duration required to approach redox equilibrium for silicate melts levitated at 1800–2100 °C was inferred to be near 30 s, based on a time series on peridotite liquids at 1800 °C, conducted in a similar device by Sossi *et al*. (2020). To further investigate the influence of experimental duration on redox equilibrium between the melt droplet and the gas stream, as well as to characterise the magnitude of evaporation of volatile elements (K, Na, P, potentially Si), time-series experiments were conducted at 2000 °C with dwell times of 10, 30, and 120 s. Experiments investigating the relationship between Fe^{3+}/Fe^{T} and temperature were conducted at 1800, 1900, 2000, and 2100 °C for 30 s.

Analytical Methods

Textures of experimentally synthesised glasses were characterised by back-scattered electron and secondary electron imaging and chemical homogeneity was validated by wavelength dispersive spectroscopy (WDS) using the JEOL JXA-8530F+ Electron Probe Microanalyzer at the University of Minnesota.

Experiments from the VF series (1300–1500 °C) were analysed by Mössbauer spectroscopy at 293 K at the Institute of Rock Magnetism, University of Minnesota as previously reported by Aithala *et al*. (2026). All spectra were fit with single, asymmetric doublets for Fe^{2+} and Fe^{3+} with correlated centre shift (CS) and quadrupole splitting (QS) parameters as recommended for glass (Alberto *et al*., 1996). Fe^{3+}/Fe^{T} was calculated from the area ratios of Fe^{2+} and Fe^{3+} corrected by the ratio of Lamb-Mössbauer factors of Fe^{3+} and Fe^{2+}, in

multicomponent silicate glasses at room temperature as determined by Roskosz *et al*. (2022; C = 1.203 ± 0.033). The Roskosz *et al.* (2022) correction factor is favoured to the Zhang *et al*. (2018) basaltic correction factor (C = 1.125 ± 0.068) as the latter is calibrated from and intended to use for terrestrial basalt compositions, which Humphrey is distinct from. However, the difference between the correction factors are small and agree within 1-σ uncertainty. Owing to their relatively small masses, material from ALLF experiments were not analysed by Mössbauer spectroscopy.

Fe K-edge XANES analyses of all VF glasses except for VF267 were reported by Aithala *et al*. (2026). ALLF glasses were analysed in one session at beamline 4-BM at the National Synchrotron Light Source—II, Brookhaven National Laboratory in which the VF glasses were reanalysed. The centroid energies measured from the reanalysed VF glasses demonstrated agreement with those from Aithala *et al*. (2026) within 0.032 eV (*e.g.*, $\Delta Fe^{3+}/Fe^{T} < 0.025$), indicating consistency and reproducibility between sessions. Procedures related to spectra collection, fitting, data normalization, and calculations for Fe^{3+}/Fe^{T} ratio and associated uncertainties using the Mössbauer-standardised martian basalt XANES calibration are described in Aithala *et al*. (2026). The ALLF glass Fe^{3+}/Fe^{T} determinations are made under the assumption that Mössbauer standardised XANES calibrations (*i.e.* Cottrell *et al*., 2009; Aithala *et al*., 2026) are applicable to glasses synthesised at the temperatures relevant to the ALLF experiments.

2. Results

Backscatter electron investigation of experimental textures reveals complete melting in all experiments except the one at lowest temperature (VF271, 1250 °C), which was apparently below the liquidus of the starting composition. Compositions of all glasses determined by WDS EPMA are given in Table S-2. Though the starting compositions of all glasses are identical, time and temperature dependent compositional variations are observed in ALLF experiment series. In particular, less refractory minor species (K, Na, P) are lost rapidly by evaporation at these elevated temperatures (Fig. S-1). The abundances of K and P also significantly deviate from the average reference composition in the VF experimental series, indicating that time-dependent evaporation of these species is prevalent, even at relatively low temperatures. The deviations of K and P in the VF series are significant relative to the reference composition, but their effect on Fe^{3+}/Fe^{T} would be negligible as their absolute mole fractions, which are of importance to quantifying non-ideal interactions between Fe and other species, are small (see SI). Other oxides (CaO-MgO-FeO-Al_2O_3-TiO_2-SiO_2) show no appreciable time-dependent variations for both the VF and ALLF series.

Fe^{3+}/Fe^{T} ratios of quenched glasses were determined by Mössbauer spectroscopy, XANES, or both (Table S-1). For the ALLF time series experiments, the Fe^{3+}/Fe^{T} ratios for experiments at 10 and 120 seconds (2000-10 and 2000-120) are equal within uncertainty, the 30 second (2000-30) result is significantly higher, and also higher than the Fe^{3+}/Fe^{T} ratio for the experiment at 1900 °C. We surmise that the experiment 2000-30 is anomalous, and that the Fe^{3+}/Fe^{T} ratios of 2000-10 and 2000-120 (0.293±0.013 and 0.294±0.013) are representative of redox equilibrium with O_2. As a result, all interpretations regarding the equilibrium composition and Fe^{3+}/Fe^{T} ratio of Humphrey in equilibrium with oxygen at 2000 °C (*e.g.*, volatile evaporation, Eqs. 7–9) are constructed based on values obtained from the 2000-10 experiment (Table S-1).

From a representative experiment temperature-time log (Fig. S-2), linear fits to the laser-off (free-quench) segment give quench rates of -641 °C s^{-1} (1900 → 1400 °C) and -500 °C s^{-1} (1600 → 1200 °C); thus the drop 1900 → 1200 °C occurs in ≈1.2 s (Fig. S-2). Even adopting a conservative upper-bound melt diffusivity (D = 1×10^{-9} m^2 s^{-1}), the diffusion length over 1.2 s is ≈61 μm, resulting in only a thin surface rind on a ~1–2 mm bead. Our 2000 °C time-series also demonstrates that redox equilibrium is achieved during the dwell (10 s and 120 s runs give indistinguishable Fe^{3+}/Fe^{T}), so the bulk redox state is set prior to quench and cannot re-equilibrate through the short high-T interval. Therefore, we conclude that the Fe^{3+}/Fe^{2+} ratios reported in Table S-1 are representative of the dwell temperatures and are quenchable under the conditions of these ALLF experiments.

3. Recalculating experiments to common oxygen fugacity and melt composition

Because the VF and ALLF experiments were equilibrated in different gas streams, air and oxygen, respectively, isolation of the effects of temperature requires recalculation to a common oxygen fugacity. We elected to recalculate the ALLF experiments to the conditions in air (log f_{O2} = -0.68). Similarly, we recalculated experiments for the effects of variations of silicate composition arising from olivine crystallization (experiment VF271) or, for the ALLF experiments, from volatile (Na, K, P) loss. These experiments were recalculated to that of the reference composition given in Table S-2.

The observed $\log\left(\frac{X_{Fe3+}}{X_{Fe2+}}\right)$ values, $\log\left(\frac{X_{Fe3+}}{X_{Fe2+}}\right)_0$, can be recalculated to common oxygen fugacity and composition, $\log\left(\frac{X_{Fe3+}}{X_{Fe2+}}\right)_C$, using an expression derived from Eq. 5,

$$\log\left(\frac{X_{Fe3+}}{X_{Fe2+}}\right)_C - \log\left(\frac{X_{Fe3+}}{X_{Fe2+}}\right)_0 = k\Delta\log f_{O2} + \sum d_i \Delta X_i \ , \qquad \text{Eq. S} - 1$$

where $\Delta\log f_{O2}$ and ΔX_i are the differences in oxygen fugacity and melt oxide mole fractions between the recalculated and unmodified experiments.

The recalculation performed in this study is based on the model established by Aithala *et al*., (2026) owing to its success in characterizing redox variations in martian magmas, and when applied to Eq. S-1 has the form,

$$\log\left(\frac{X_{Fe3+}}{X_{Fe2+}}\right)_C = \log\left(\frac{X_{Fe3+}}{X_{Fe2+}}\right)_0 + k\Delta\log f_{O2} + d_{K_2O}\left(\Delta X_{K_2O}\right), \quad \text{Eq. S} - 2$$

where the coefficients of k and d_{K2O} (0.1988, -99.62) are adopted from Aithala *et al*. (2026). Owing to previous work finding compositional components in addition to K_2O being significant in modifying the ratio of Fe^{3+}/Fe^{2+} at given f_{O2}, T, and P, we present, also, an alternative compositional recalculation using the model Borisov *et al*., (2018) which has the form,

$$\log\left(\frac{X_{\mathrm{Fe3+}}}{X_{\mathrm{Fe2+}}}\right)_C = \log\left(\frac{X_{\mathrm{Fe3+}}}{X_{Fe2+}}\right)_0 + 0.1988\Delta\log f_{\mathrm{O2}} - 0.445\left(\Delta X_{\mathrm{K_2O}}\right) - 0.900\left(\Delta X_{\mathrm{TiO_2}}\right) + 1.532\left(\Delta X_{\mathrm{MgO}}\right) + 0.314\left(\Delta X_{\mathrm{CaO}}\right) + 2.030\left(\Delta X_{\mathrm{Na_2O}}\right) + 3.355\left(\Delta X_{\mathrm{K_2O}}\right) - 4.851\left(\Delta X_{\mathrm{P_2O_5}}\right) - 3.081\left(\Delta X_{\mathrm{SiO_2}} X_{\mathrm{Al_2O_3}}\right) - 4.370\left(\Delta X_{\mathrm{SiO_2}} X_{\mathrm{MgO}}\right). \quad \text{Eq. S} - 3$$

Note that the *k*-value of 0.1988 is maintained from Aithala *et al*. (2026) as it is the most accurate *k*-value for describing Fe^{3+}/Fe^{2+} variations in martian magmas. Recalculated Fe^{3+}/Fe^{2+} ratios determined by Eqs. S-2 and S-3 are reported in Table S-3.

4. Applying temperature Eqs. 7–9 to model silicate liquids of differing compositions and f_{O2}s

Equations 7–9 in the main text are derived from regression analysis of the Fe^{3+}/Fe^{2+} ratios of silicate glasses that are compositionally similar to martian basaltic glasses and synthesised at comparatively oxidizing conditions. Therefore, it is important to address whether these models can be extrapolated and applied for the scenarios presented in the Discussion section of the main text: specifically, for better constraining the role of temperature on Fe-redox state of reduced magmas (*i.e.* Mars and magma oceans), as well as to magmas of differing composition (*i.e.* ultramafic magma ocean liquids). While the experiments presented are not conducted at the same conditions as the scenarios modelled, and further high temperature experiments spanning a wider range of conditions are desirable, the first-order influence of temperature on Fe^{3+}/Fe^{2+} resides in standard state properties that do not depend on composition or the Fe^{3+}/Fe^{2+} ratio, and so until further data become available, the application of the temperature dependence determined here is reasonable.

Based on Eq. 2 at 100 kPa, $\log\left(\frac{X_{\mathrm{Fe3+}}}{X_{\mathrm{Fe2+}}}\right)$ depends on $\log f_{O2}$, $\frac{\Delta G_{T,P_0}}{T}$, and $\log\left(\frac{\gamma^{melt}_{Fe3+}}{\gamma^{melt}_{Fe2+}}\right)$. $\log f_{O2}$ is an intensive parameter independent of temperature, leaving $\frac{\Delta G_{T,P_0}}{T}$, and $\log\left(\frac{\gamma^{melt}_{\mathrm{Fe3+}}}{\gamma^{melt}_{\mathrm{Fe2+}}}\right)$ as the terms that potentially define the temperature dependence of $\log\left(\frac{X_{\mathrm{Fe3+}}}{X_{\mathrm{Fe2+}}}\right)$ in silicate melts. The $\Delta G_{T,P_0}$ term, referring to the difference in the free energies of formation between pure $FeO_{1.5}$ and FeO components are, by definition, independent of the relative abundance of $FeO_{1.5}$, FeO, and other melt components. Therefore, experiments on any Fe-bearing silicate melt composition, investigated at any f_{O2} across a range of temperatures could be leveraged to constrain the form of $\Delta G_{T,P_0}$ at 100 kPa.

The temperature dependence of the $\log\left(\frac{\gamma^{melt}_{Fe3+}}{\gamma^{melt}_{Fe2+}}\right)$ term (i.e., the "non-ideal" interactions between Fe^{3+}, Fe^{2+} and other melt components) is more challenging to define, as its form is dependent on the solution model used for its approximation (see Borisov *et al.,* 2015). Many previous studies investigating Fe^{3+}/Fe^{T} in silicate melts, however, have chosen not to ascribe a temperature dependence to the compositional terms (for example, there is no temperature dependence to the $\sum d_i X_i$ terms in the models parameterised Kress and Carmichael, 1991; Righter *et al.,* 2013; Borisov *et al.,* 2018). Jayasuriya *et al.* (2004) and Hirschmann (2022) incorporate simple temperature-dependences to their compositional terms, based on theory that the contribution of non-ideal interactions to Fe^{3+}/Fe^{2+} should decrease with increasing temperature, but these effects were found to be small. In fact, Jayasuriya *et al*. (2004) found that fits to experimental Fe^{3+}/Fe^{2+} ratios were improved when the

temperature-dependence of compositional components were entirely ignored, further highlighting its insignificance for the temperature-dependent behaviour of Fe^{3+}/Fe^{2+} when compared to the $\Delta G_{T,P_0}$ term.

The thermodynamic arguments above validate that Eqs. 7–9 can be applied to the shergottite and magma ocean liquids modelled in the Discussion as the differences in composition and f_{O2} of investigation should not affect the role of temperature in calculating f_{O2} evolution during cooling and the differences in Fe^{3+}/Fe^{2+} ratios at fixed f_{O2} at a range of temperatures. The temperature dependence of Fe^{3+}/Fe^{2+} ratio as a function of temperature can theoretically be determined at any f_{O2} of choice, however, the practical advantage in determining the temperature dependence at relatively oxidizing conditions is that differences in Fe^{3+}/Fe^{2+} are large in magnitude for a given change in temperature. At f_{O2} extremes—where the melt contains nearly 100 % FeO or $FeO_{1.5}$—Fe^{3+}/Fe^{2+} (or specifically, $\log\left(\frac{X_{Fe3+}}{X_{Fe2+}}\right)$) variations due to temperature may not be resolvable relative to the uncertainties of existing analytical techniques. This can be observed in the temperature series of Righter *et al*. (2013), where martian magma compositions were investigated from 1300–1500 °C at f_{O2} of QFM and 0.8 GPa of pressure. The Fe^{3+}/Fe^{T} ratios measured from this series range from 0.02–0.03 with analytical uncertainties of ±0.025 with no discernible trend with temperature. While the noted lack of dependence between Fe^{3+}/Fe^{T} and temperature at fixed f_{O2} relative to QFM presented by Righter *et al*. (2013) could potentially be accurate, the large uncertainties relative to their measurements make that conclusion less certain (note: the f_{O2} of QFM changes across temperature, making the Righter *et al*. (2013) series not directly comparable to the VF and ALLF series that are at fixed at absolute f_{O2} of air and O_2). The Fe^{3+}/Fe^{T} uncertainties in the Righter *et al*. (2013) experiments manifest as large errors in $\log\left(\frac{X_{Fe3+}}{X_{Fe2+}}\right)$ at $Fe^{3+}/Fe^{T} < 0.05$ which leads to imprecise characterization of the relationship between $\log\left(\frac{X_{Fe3+}}{X_{Fe2+}}\right)$ and inverse temperature, resulting in their *h*-coefficient to be weakly constrained. This may potentially explain why the *h*-coefficient obtained by Righter *et al*. (2013) significantly deviates from all previously established *h*-coefficients.

Supplementary Tables

Table S-1 Run table.

Series	ID	Temperature (°C)	duration	logf_{O2}	XANES Centroid (eV)	Fe^{3+}/Fe^{T}	
						XANESs	Mössbauer
Vertical Furnace	VF271	1250	72 h	-0.68	7113.425±0.008	0.816±0.019	-
	VF267	1300	24 h	-0.68	-	-	0.736±0.023
	VF231	1365	6 h	-0.68	7113.317±0.008	0.726±0.016	0.716±0.023
	VF268	1400	6 h	-0.68	7113.220±0.016	0.650±0.017	0.695±0.023
	VF270	1450	2 h	-0.68	7113.264±0.012	0.685±0.016	0.661±0.023
	VF274	1500	1 h	-0.68	7113.203±0.005	0.637±0.012	0.643±0.023
ALLF Temp. Series	1800-30	1800	30 s	0	7112.890±0.023	0.426±0.018	-
	1900-30	1900	30 s	0	7112.828±0.027	0.389±0.019	-
	2000-30	2000	30 s	0	7112.859±0.050	0.407±0.031	-
	2100-30	2100	30 s	0	7112.674±0.031	0.306±0.018	-
ALLF Time Series	2000-10	2000	10 s	0	7112.808±0.017	0.378±0.015	-
	2000-120	2000	120 s	0	7112.809±0.016	0.378±0.015	-

Table S-2 WDS table.

Series	ID	SiO_2	TiO_2	Al_2O_3	FeO*	MgO	CaO	Na_2O	K_2O	P_2O_5
Vertical Furnace	VF271	51.55±0.54	0.50±0.04	11.65±0.08	12.07±0.10	11.00±0.17	8.32±0.04	3.07±0.03	0.05±0.01	0.30±0.03
	VF267	50.79±1.00	0.54±0.05	9.98±0.12	14.26±0.16	11.66±0.07	6.85±0.04	3.05±0.03	0.06±0.005	0.27±0.01
	VF231	47.20±0.23	0.49±0.03	10.68±0.13	15.94±0.10	11.81±0.07	7.67±0.03	3.28±0.03	0.04±0.009	0.48±0.03
	VF268	47.99±0.80	0.49±0.04	10.95±0.18	14.94±0.12	12.40±0.28	7.67±0.03	2.72±0.09	0.06±0.008	0.27±0.02
	VF270	47.96±0.55	0.52±0.02	11.04±0.08	14.87±0.10	12.43±0.12	7.66±0.04	3.00±0.03	0.05±0.01	0.35±0.03
	VF274	47.92±0.37	0.49±0.05	11.16±0.08	15.04±0.12	12.48±0.06	7.76±0.04	3.06±0.04	0.07±0.006	0.29±0.03
ALLF Temp. Series	1800-30	47.24±0.52	0.53±0.05	11.32±0.11	16.04±0.21	12.54±0.12	7.88±0.04	1.98±0.03	0.029±0.006	0.13±0.04
	1900-30	47.97±0.29	0.52±0.04	11.44±0.14	15.79±0.18	12.64±0.09	7.88±0.04	1.68±0.05	0.024±0.007	0.039±0.017
	2000-30	48.41±0.27	0.55±0.02	11.52±0.08	15.68±0.20	12.60±0.15	7.94±0.07	1.61±0.04	0.021±0.004	0.032±0.017
	2100-30	49.17±0.32	0.55±0.05	11.75±0.13	15.01±0.12	12.96±0.19	8.12±0.04	0.68±0.01	0.008±0.004	0.013±0.01
ALLF Time Series	2000-10	47.76±0.42	0.52±0.05	11.37±0.13	15.93±0.18	12.60±0.13	7.80±0.03	2.03±0.06	0.039±0.004	0.274±0.08
	2000-120	48.73±0.36	0.54±0.03	11.70±0.09	15.33±0.18	13.04±0.13	8.05±0.05	0.94±0.03	0.009±0.006	0.018±0.014
Ref. Comp.[a]		47.77±1.39	0.50±0.02	10.96±0.47	15.20±0.60	12.28±0.39	7.69±0.38	3.01±0.20	0.055±0.010	0.347±0.09

[a] Reference composition calculated by averaging composition of VF267, VF231, VF268. VF270, and VF274

Table S-3 Experiment Fe^{3+}/Fe^{T} and recalculations.

Series	ID	Fe^{3+}/Fe^{T}—raw	Fe^{3+}/Fe^{T}—air recalculatedd	Fe^{3+}/Fe^{T}—A_sub.[a]	Fe^{3+}/Fe^{T}—B18[b]
Vertical Furnace	VF271	0.816±0.022	-	0.815±0.023	0.801±0.024
	VF267	0.736±0.023	-	-	-
	VF231	0.716±0.023	-	-	-
	VF268	0.695±0.023	-	-	-
	VF270	0.661±0.023	-	-	-
	VF274	0.643±0.023	-	-	-
ALLF Temp. Series	1800-30	0.426±0.018	0.352±0.017	0.343±0.017	0.344±0.017
	1900-30	0.389±0.019	0.318±0.017	0.308±0.017	0.304±0.017
	2000-30	0.407±0.031	0.335±0.027	0.323±0.027	0.317±0.027
	2100-30	0.306±0.018	0.244±0.014	0.231±0.014	0.216±0.014
ALLF Time Series	2000-10	0.378±0.015	0.308±0.014	0.303±0.014	0.297±0.014
	2000-120	0.378±0.015	0.308±0.014	0.294±0.014	0.282±0.014

Notes: ALLF experiments' Fe^{3+}/Fe^{T} are adjusted to air ($\log f_{O2}$ = -0.68) to compare to VF experiments. Compositional recalculations, calculated from the Aithala *et al*. (2026)[a] and Borisov *et al*. (2018)[b] models, are applied to experiments exhibiting significant deviation from the averaged reference composition (Table S-2) based on air Fe^{3+}/Fe^{T} ratios. See SI (section 3) for calculation details.

Table S-4 Equation 6 fit coefficients

	h (K)	ΔC_P (J/K)	*c*	X^2	r-X^2
Eq. 7.	4894±232.5	-	-2.581±0.1241	20.2	2.53
Eq. 8.	5235±243.4	33.25*	-2.786±0.1296	23.4	2.92
Eq. 9.	4511±691.7	-23.74±51.05	-2.349±0.4117	20.2	2.88

Notes: ΔC_P is fixed at 33.25 J/K determined by Hirschmann (2022).

Table S-5 Compilation of superliquidus experimental series displayed in Figure 3. All were conducted in air at constant composition and variable temperature.

Source[a]	Temperature Series	n[b]	Temperature Range (°C)	h[c] (K)	SiO_2 (wt. %)	FeO* (wt. %)
Present Study	**Humphrey**	**10**	**1250–2100**	**4894±232.5**	**47.77**	**15.20**
Ken48	NMF	3	1200–1400	4717±23.41	50.87	11.32
Kil83	121	2	1344–1445	-909.0*	71.78	7.93
	3114	2	1340–1454	6582*	69.37	5.93
	20424	2	1342–1447	7865*	39.41	11.75
	780-U-105	2	1350–1445	2820*	40.00	13.42
	780-U-111	2	1344–1445	7082*	44.15	11.68
	CAM-49	2	1342–1434	264.1*	72.29	1.63
	IC-2	4	1342–1443	-1960±406	73.76	3.24
	NIC-8	2	1344–1430	4198*	61.51	5.91
KC88	JDFD-2	8	1360–1635	5067±572.0	50.81	11.94
M95	MAS	8	1215–1550	7166±656.1	54.91	5.84
	NZC	9	1250–1557	7754±1026	74.6	5.07
BM2010	DAF_BM	4	1398–1571	4723±236.3	47.9	4.68
	DAFL	2	1424–1540	3909*	50.3	0.99
	DAS20F	4	1398–1571	4410±101.1	53.2	4.59
	DAS40F	4	1398–1571	3866±282.8	58.5	4.68
	DAS60F	4	1398–1571	5115±441.8	63.7	4.59
	DAS80F	3	1450–1571	5058±22.17	69.1	4.59
B13-18	DAF	20	1399–1551	5102±321.9	45.56	8.78
	DAF20	4	1399–1550	5513±277.4	40.42	17.42
	DAF5	4	1399–1550	4437±871.2	48.05	4.2
	DAFA22	3	1450–1551	4272±426.4	41.06	8.7
	DAFA30	3	1450–1551	4485±188.1	36.42	8.96
	DAFM15	2	1501–1551	4854*	42.79	8.78
	DAFM20	2	1501–1551	5566*	39.93	8.76
	DAFN15/DAFSK25	2	1450–1500	1100*	52.72	7.5
	DAFN8/HAFSK13	2	1450–1499	4798*	49.68	7.82
	DAFOL20	3	1450–1550	5117±87.86	44.95	8.6
	DAFOL40	3	1450–1550	4742±41.15	44.38	8.62
	DAFP05	3	1451–1552	4921±52.67	43.3	8.76
	DAFP10	3	1451–1552	4983±125.3	40.77	8.74
	DAFP15	3	1451–1552	4796±123.3	38.41	8.77
	DAFP20	3	1451–1552	4703±68.32	36.43	8.72

B13-18 contd.	DAFS	15	1450–1551	5817±892.8	65.67	8.92
	DAFSA15	3	1450–1551	5409±227.6	60.05	8.73
	DAFSA23	3	1450–1551	4392±208.1	54.08	8.8
	DAFSM13	2	1501–1551	5113*	60.58	9.06
	DAFSM21	2	1501–1551	4983*	54.4	9.07
	DAFSN15/DAFSK25	2	1450–1500	488.8*	56.7	7.49
	DAFSP08	4	1501–1552	4339±610.6	51.06	8.81
	DAFST15	2	1451–1502	8100*	55.44	8.43
	DAFST25	2	1178–1229	5641*	47.33	8.8
	DAFT10	3	1400–1502	6824±1041	40.8	8.45
	DAFT20	3	1400–1502	6270±1082	35.04	8.56
	DAFT30	3	1400–1502	5866±873.5	30.41	8.62
	HAF	3	1450–1553	5009±529.4	56.14	9.03
	HAFC11	2	1500–1553	5375*	49.3	8.94
	HAFC11S	2	1500–1553	4948*	61.48	8.67
	HAFC16	3	1450–1553	4826±247.2	45.92	9.05
	HAFC16S	2	1500–1553	4093*	60.24	8.93
	HAFC5	2	1500–1553	4826*	52.54	9.52
	HAFC5S	2	1500–1553	3176*	63.22	9.04
	HAFS	5	1500–1553	10190±4510	63.06	8.8
	HRF10	4	1301–1451	4145±158.7	57.5	8.85
	HRF20	4	1301–1451	3938±163.2	51.25	17.9
	HRF5	4	1301–1451	4595±217.0	60.12	5.05
	SAF	3	1398–1499	4428±102.7	64.88	8.75
	SAFM10	2	1448–1449	4903*	58.56	8.53
	SAFM15	2	1448–1499	4963*	55.04	8.69
	SAFM5	3	1398–1499	4632±18.05	61.8	8.53

Notes: [a]Ken48: Kennedy (1948), Kil83: Kilinc *et al*. 1983, KC88: Kress and Carmichael (1988), M95: Moore *et al*. (1995), BM2010: Borisov and McCammon (2010), B13-18: Borisov *et al*. (2013, 2015, 2017, 2018).[b]*n* is the number of experiments in a given series. [c]*h* refers to the regressed slope of $\mathbf{log}\left(\frac{X_{Fe3+}}{X_{Fe2+}}\right)$ vs. T^{-1} (K^{-1}) with 1-σ uncertainties. *Denotes series comprising of only two experiments.

Supplementary Figures

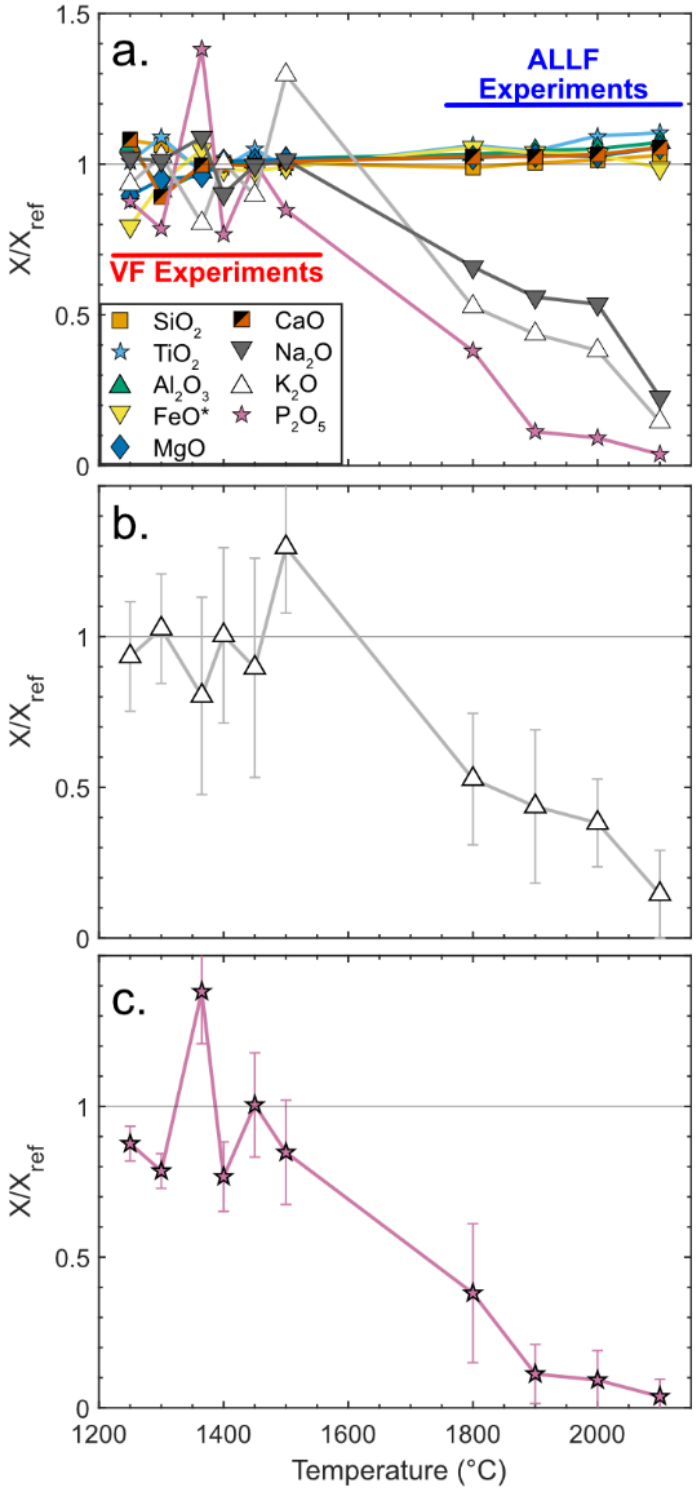

Figure S-1 Compositional variation as a function of experimental temperature relative to the reference composition (Table S-2), as calculated by the ratio of their mole fractions (X/X_{ref}). **(a)**: all components, **(b)**: K_2O with 2-σ error bars, **(c)**: P_2O_5 with 2-σ error bars.

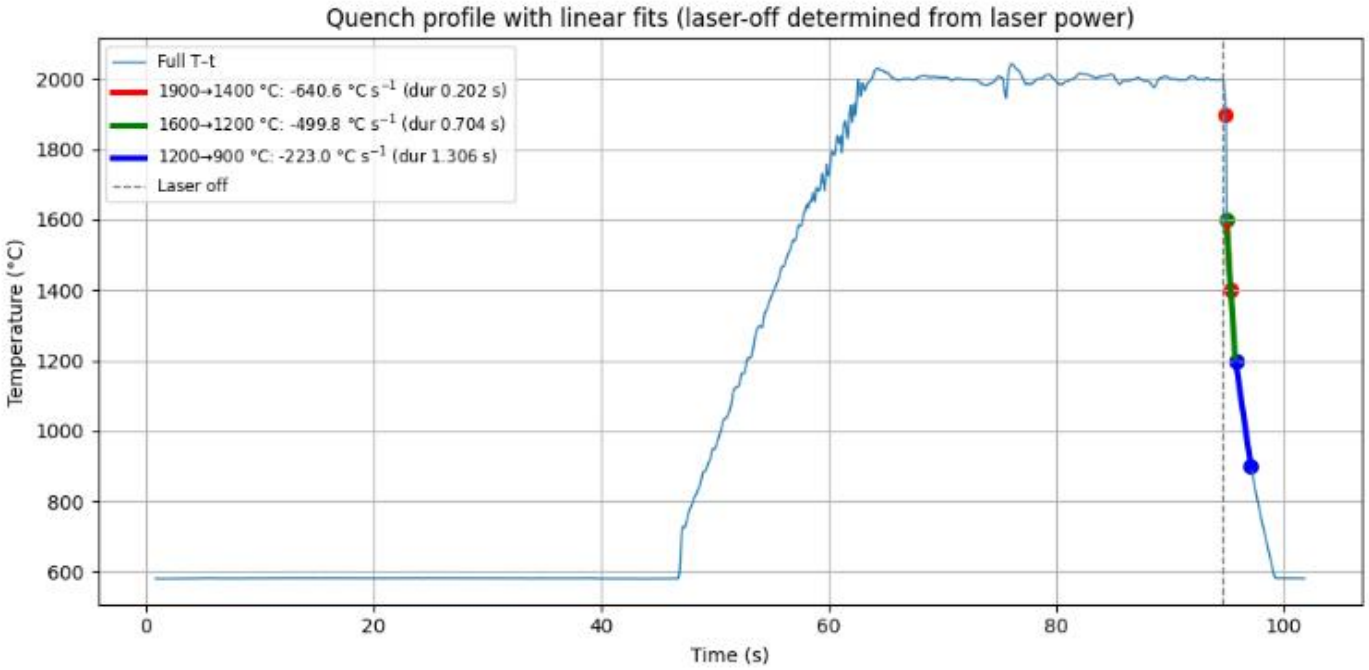

Figure S-2 Representative temperature-time log from ALLF experiment 2000-30 obtained from pyrometer measurements throughout the experimental runtime. The quench profile begins at vertical dashed line (laser off) and quench rates are calculated using linear fits from 1900–1400 °C, 1600–1200 °C, and 1200–900 °C.

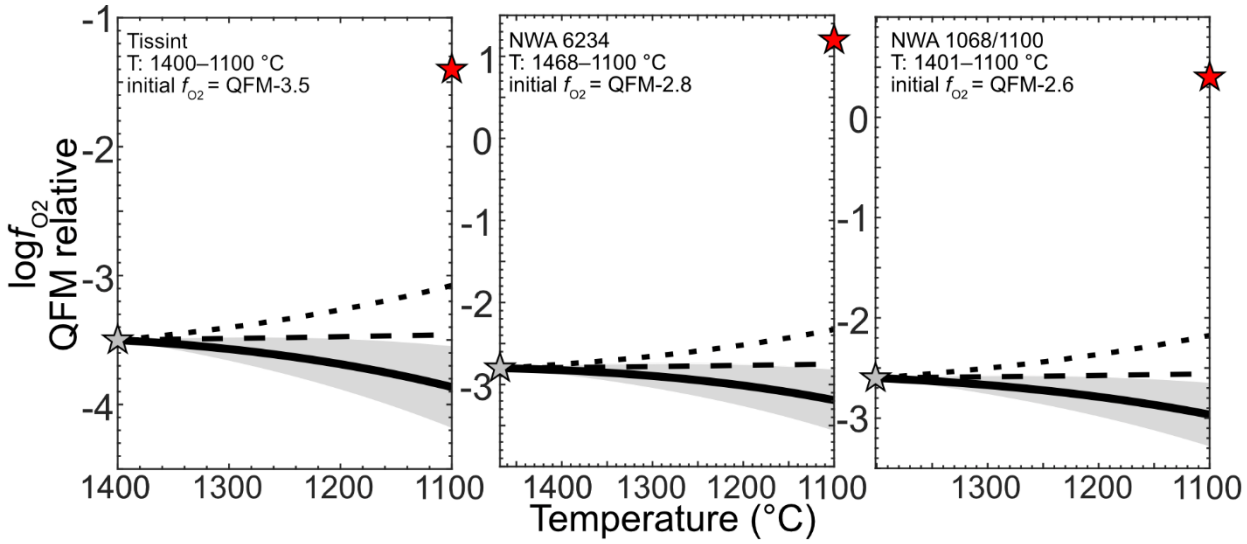

Figure S-3 Calculated f_{O2} change during unbuffered, isochemical cooling of shergottite liquids Tissint, NWA 6234, and NWA 1068/1100 from liquidus to 1100 °C as calculated by Eqs. 8 (solid black line with shaded area representing 2-σ uncertainties for the *h*-coefficient), 7 (long dashes), and 9 (short dashes).

Supplementary Information References

Aithala, S.P., Lange, R.A., Hirschmann, M.M. (2026) Controls on iron-redox state in martian magmas quantified by Mössbauer spectroscopy, colorimetric wet chemistry, and XANES spectroscopy. *Journal of Geophysical Research: Planets* 131, e2025JE009148. https://doi.org/10.1029/2025JE009148

Biren, J., Slodczyk, A., Andújar, J., del Campo, L., Cosson, L., Li, H., *et al.* (2022) High temperature spectral emissivity of glass and crystal-bearing basalts. *Journal of Volcanology and Geothermal Research* 430, 107623. https://doi.org/10.1016/j.jvolgeores.2022.107623

Borisov, A., Behrens, H., Holtz, F. (2013) The effect of titanium and phosphorus on ferric/ferrous ratio in silicate melts: An experimental study. *Contributions to Mineralogy and Petrology* 166, 1577–1591. https://doi.org/10.1007/s00410-013-0943-9

Borisov, A., Behrens, H., Holtz, F. (2015) Effects of melt composition on Fe3+/Fe2+ in silicate melts: A step to model ferric/ferrous ratio in multicomponent systems. *Contributions to Mineralogy and Petrology* 169, 24. https://doi.org/10.1007/s00410-015-1119-6

Borisov, A., Behrens, H., Holtz, F. (2017) Effects of strong network modifiers on Fe3+/Fe2+ in silicate melts: An experimental study. *Contributions to Mineralogy and Petrology* 172, 34 https://doi.org/10.1007/s00410-017-1337-1

Borisov, A., Behrens, H., Holtz, F. (2018) Ferric/ferrous ratio in silicate melts: A new model for 1 atm data with special emphasis on the effects of melt composition. *Contributions to Mineralogy and Petrology* 173, 98 https://doi.org/10.1007/s00410-018-1524-8

Borisov, A., McCammon, C. (2010) The effect of silica on ferric/ferrous ratio in silicate melts: An experimental study using Mossbauer spectroscopy. *American Mineralogist* 95, 545–555. https://doi.org/10.2138/am.2010.3217

Cottrell, E., Kelley, K.A., Lanzirotti, A., Fischer, R.A. (2009) High-precision determination of iron oxidation state in silicate glasses using XANES. Chemical Geology 268, 167–179. https://doi.org/10.1016/j.chemgeo.2009.08.008

Deng, J., Du, Z., Karki, B.B., Ghosh, D.B., Lee, K.K.M. (2020) A magma ocean origin to divergent redox evolutions of rocky planetary bodies and early atmospheres. *Nature Communications* 11, 2007. https://doi.org/10.1038/s41467-020-15757-0

Dyar, M.D., Helbert, J., Treiman, A.H. (2017) *Near-infrared emissivity of silicate rocks at Venus temperatures*. 15th VEXAG Meeting, Abstract and Presentation.

Dyar, M.D., Treiman, A.H., Helbert, J., Filiberto, J. (2019a) *Planetary emissivity measurements at high temperature: Implications for Venus and remote sensing*. VEXAG Presentation to the Planetary Science Advisory Committee, Slide 14.

Dyar, M.D., Treiman, A.H., Helbert, J., Filiberto, J. (2019b) *Planetary emissivity measurements at high temperature: Progress and new data*. AGU Fall Meeting Abstract P14B-08.

Helbert, J., Dyar, M.D., Treiman, A.H. (2017) *Laboratory measurements of basalt emissivity at Venus surface temperatures*. 48th Lunar and Planetary Science Conference, Abstract #1512.

Hirschmann, M.M. (2021) Iron-wüstite revisited: A revised calibration accounting for variable stoichiometry and the effects of pressure. *Geochimica et Cosmochimica Acta* 313, 74–84. https://doi.org/10.1016/j.gca.2021.08.039

Hirschmann, M.M. (2022) Magma oceans, iron and chromium redox, and the origin of comparatively oxidized planetary mantles. *Geochimica et Cosmochimica Acta* 328, 221–241. https://doi.org/10.1016/j.gca.2022.04.005

Jayasuriya, K.D., O'Neill, H.St.C., Berry, A.J., Campbell, S.J. (2004) A Mössbauer study of the oxidation state of Fe in silicate melts. *American Mineralogist* 89, 1597–1609. https://doi.org/10.2138/am-2004-11-1203

Kennedy, G.C. (1948) Equilibrium between volatiles and iron oxides in igneous rocks. *American Journal of Science* 246, 529–548. https://doi.org/10.2475/ajs.246.9.529

Kilinc, A., Carmichael, I.S.E., Rivers, M.L., Sack, R.O. (1983) The ferric-ferrous ratio of natural silicate liquids equilibrated in air. *Contributions to Mineralogy and Petrology* 83, 136–140. https://doi.org/10.1007/bf00373086

Kress, V.C. and Carmichael, I.S.E. (1988) Stoichiometry of the iron oxidation reaction in silicate melts. *American Mineralogist* 73, 1267–1274.

Kress, V.C., Carmichael, I.S.E. (1991) The compressibility of silicate liquids containing Fe_2O_3 and the effect of composition, temperature, oxygen fugacity and pressure on their redox states. *Contributions to Mineralogy and Petrology* 108, 82–92. https://doi.org/10.1007/Bf00307328

Lombardo, V., Pick, L., Spinetti, C., Taddeucci, J., Zakšek, K. (2020) Temperature and emissivity separation "draping" algorithm applied to hyperspectral infrared data. *Remote Sensing* 12, 2046. https://doi.org/10.3390/rs12122046

McSween, H.Y., Ruff, S.W., Morris, R.V., Bell, J.F., Herkenhoff, K., Gellert, R., Stockstill, K.R., Tornabene, L.L., Squyres, S.W., Crisp, J.A., Christensen, P.R., McCoy, T.J., Mittlefehldt, D.W., Schmidt, M. (2006) Alkaline volcanic rocks from the Columbia Hills, Gusev crater, Mars. *Journal of Geophysical Research: Planets* 111, E09S91. https://doi.org/10.1029/2006je002698

Moore, G., Righter, K., Carmichael, I.S.E. (1995) The effect of dissolved water on the oxidation state of iron in natural silicate liquids. *Contributions to Mineralogy and Petrology* 120, 170–179 https://doi.org/10.1007/BF00287114

Ni, P., Macris, C.A., Darling, E.A., Shahar, A. (2021) Evaporation-induced copper isotope fractionation: Insights from laser levitation experiments. *Geochimica et Cosmochimica Acta* 298, 131–148. https://doi.org/10.1016/j.gca.2021.02.007

Roskosz, M., Dauphas, N., Hu, J., Hu, M.Y., Neuville, D.R., Brown, D., Bi, W., Nie, N.X., Zhao, J., Alp, E.E. (2022) Structural, redox and isotopic behaviors of iron in geological silicate glasses: A NRIXS study of Lamb-Mössbauer factors and force constants. *Geochimica et Cosmochimica Acta* 321, 184–205. https://doi.org/10.1016/j.gca.2022.01.021

Sossi, P.A., Burnham, A.D., Badro, J., Lanzirotti, A., Newville, M., O'Neill, H.St.C. (2020) Redox state of Earth's magma ocean and its Venus-like early atmosphere. *Science Advances* 6, eabd1387. https://doi.org/10.1126/sciadv.abd1387

Treiman, A.H., Filiberto, J., Vander Kaaden, K.E. (2019) Near-infrared reflectance spectroscopy of Venus-analog rocks at Venus surface temperatures. *17th Venus Exploration Analysis Group Meeting, Abstract #13*. https://ntrs.nasa.gov/api/citations/20190032647/downloads/20190032647.pdf

Young, E.D., Macris, C.A., Tang, H., Hogan, A.A., Shollenberger, Q.R. (2022) Isotope velocimetry: Experimental and theoretical demonstration of the potential importance of gas flow for isotope fractionation during evaporation of protoplanetary material. *Earth and Planetary Science Letters* 589, 117575. https://doi.org/10.1016/j.epsl.2022.117575